Effect of Small-scale Topography on Eddy Dissipation in the Northern South China Sea

ZHIBIN YANG,[a] ZHAO JING, [a, b, c] XIAOMING ZHAI, [d]

[a] *Frontier Science Center for Deep Ocean Multispheres and Earth System (FDOMES) and Physical Oceanography Laboratory, Ocean University of China, Qingdao, China.*

[b] *Qingdao National Laboratory for Marine Science and Technology, Qingdao, China.*

[c] *International Laboratory for High-Resolution Earth System Prediction, Texas A&M University, College Station, Texas*

[d] *Centre for Ocean and Atmospheric Sciences, School of Environmental Sciences, University of East Anglia, Norwich, United Kingdom*

Corresponding author: Zhao Jing, jingzhao198763@sina.com

Xiaoming Zhai, xiaoming.zhai@uea.ac.uk

Abstract

Mesoscale eddies are ubiquitous dynamical features, accounting for over 90% of the total kinetic energy of the ocean. However, the pathway for eddy energy dissipation has not been fully understood. Here we investigate the effect of small-scale topography on eddy dissipation in the northern South China Sea by comparing high-resolution ocean simulations with smooth and synthetically-generated rough topography. The presence of rough topography is found to (1) significantly enhance viscous dissipation and instabilities within a few hundred meters above the rough bottom, especially in the slope region, and (2) change the relative importance of energy dissipation by bottom frictional drag and interior viscosity. The role of lee wave generation in eddy energy dissipation is investigated using a Lagrangian filter method. About one-third of the enhanced viscous energy dissipation in the rough topography experiment is associated with lee wave energy dissipation, with the remaining two-thirds explained by nonwave energy dissipation, at least partly as a result of the nonpropagating form drag effect.

1. Introduction

Mesoscale eddies, accounting for over 90% of the total kinetic energy of the oceans (Ferrari and Wunsch 2009), play an important role in the climate system by transporting heat, fresh water and carbon around the globe (Chelton et al., 2011). They are generated primarily through instabilities of the mean currents (e.g., Gill et al. 1974; Wunsch 1998; Zhai and Marshall 2013). Yet how these eddies are dissipated remains one of the largest uncertainties in the ocean energy budget (Ferrari and Wunsch 2009).

Satellite altimetry observations suggest that the western boundary of the ocean basin acts as a "graveyard" for westward-propagating ocean eddies (Zhai et al. 2010). However, the physical processes responsible for eddy energy loss remain ambiguous. The potential candidates for dissipating eddy energy include direct damping by air-sea interactions (Duhaut and Straub 2006; Zhai and Greatbatch 2007; Hughes and Wilson 2008; Ma et al. 2016; Xu et al. 2016), bottom frictional drag (Sen et al. 2008; Arbic et al. 2009), loss of balance (Molemaker et al. 2005; Williams et al. 2008; Alford et al. 2013), and energy transfer to lee waves over rough bottom topography (Nikurashin and Ferrari 2010a; Nikurashin et al. 2013). It has been found that energy dissipation caused by bottom friction is elevated near the western boundary, but it is still insufficient to explain the eddy dissipation in that region (Wright et al. 2012), suggesting that other physical processes such as lee wave generation and energy dissipation may have a more important role to play. The generation of lee wave over rough topography often leads to bottom-enhanced diapycnal mixing. There are fragments of evidence suggesting bottom-enhanced diapycnal mixing near the western boundary of the North Atlantic (Walter et al. 2005; Stöber et al. 2008) which may be associated with lee wave generation over rough topography.

Using an idealized model, Yang et al. (2021) investigated the energetics of eddy-western boundary interaction with a particular focus on the effect of small-scale bottom topography. They found that eddy kinetic energy dissipation at the western boundary is significantly enhanced in the presence of rough topography, as a result of greater anticyclonic, ageostrophic instability (AAI). The significance of the western boundary is that it brings the seabed upward to the surface and as such it enables the rough topography to be in close contact with the energetic part of the surface intensified eddies. However, the model used by Yang et al. (2021) is highly idealized; it has neither background flow nor external atmospheric forcing and it excludes large-scale topographic features. The large-scale topography[1], on the other hand, can not only accelerate the bottom flow downstream, but also block the flow upstream and lead to energy dissipation through the so-called nonpropagating form drag effect (Klymak 2018; Klymak et al. 2021). In addition, the horizontal current velocity near the ocean bottom, a key parameter in determining whether lee waves radiate or not, tends to be somewhat weak in the model experiments of Yang et al. (2021) which simulate free decay of an initial eddy field. Further studies are therefore required to improve our understanding of the role of small-scale topography in dissipating eddy energy in the ocean.

Here we conduct a high-resolution realistic model study of the effect of small-scale topography on eddy dissipation in the northern South China Sea (SCS). The SCS is the largest semi-enclosed marginal sea in the northwest Pacific (Figure 1), with its circulation relatively independent of the surrounding water. A large number of mesoscale eddies have been observed in the northern SCS and many of them appear to dissipate over the western boundary slope (Yang et al. 2019). This makes the northern SCS an ideal region to study the effect of small-scale topography on eddy dissipation. We begin in section 2 by describing the model setup and experimental design. In section 3, we compare results from model experiments with and without small-scale rough topography and then present a case study of eddy-topography interaction. Effects of nonpropagating form drag and tides are discussed in section 4. Finally, the paper concludes with a summary in section 5.

---

[1] Here "large-scale" refers to horizontal scales larger than the radiating lee wave scales ($|U_0/f|$ to U_0/N, where U_0 is the bottom velocity, f is the inertial frequency and N is the bottom stratification), and "small-scale" refers to scales in the range of the radiating lee wave scales.

2. Methodology

2.1. Model configurations

The Massachusetts Institute of Technology general circulation model (MITgcm; Marshall et al. 1997) with hydrostatic configuration is adopted to simulate mesoscale eddies and their dissipation in the northern SCS. We use a nested modelling system, ranging from a parent grid with a resolution of Δx = 1/24° (hereinafter P1) covering most of the Northwest Pacific to successive child grids with Δx = 1/72° for the SCS (hereinafter C1) and Δx = 1/216° for the northern SCS (hereinafter C2, Figure 1). The nesting procedure is one way and offline. For all three nested models the harmonic Leith and modified bi-harmonic Leith coefficients are set to be 1.2 and 1.5. The original Leith viscosity only removes vorticity buildup at the grid scale. Thus, a divergent flow with little or no vertical vorticity can be undamped. The modified version of Leith viscosity fixes this problem by adding a damping of the divergent velocity (Ilıcak 2016). The bi-harmonic temperature/salinity diffusion coefficient is chosen to be 1×10^{8} m^{4} s^{-1} at 1/24° resolution and reduced by a factor of ten for each tripling in resolution. No harmonic horizontal diffusivity is used. We employ the K-profile parameterization (KPP) vertical mixing scheme (Large et al. 1994) and a quadratic bottom friction with a drag coefficient of C_d = 0.0021. P1 and C1 are driven by daily atmospheric forcing constructed from climatology outputs of ERA-Interim (Dee et al. 2011). The atmospheric forcing for C2 is the same as P1 and C1, except that the monthly-varying ERA-Interim wind forcing is used in order to eliminate the generation of wind-induced near-inertial waves. There is no tidal forcing applied at the model lateral boundaries.

The P1 domain has a 41° × 32° horizontal extent (99°E – 140°E, 2°S – 30°N) with the bottom topography constructed from the SRTM30_PLUS dataset with a grid size of 1/120° (Becker et al. 2009). There are 83 vertical levels whose thickness increase from 1 m near the surface to 257 m near the bottom. The initial and boundary temperature and salinity fields are obtained from the World Ocean Atlas (WOA, Conkright et al. 2002), and the boundary velocity is taken from the monthly-averaged

SODA ocean climatology outputs (Carton and Giese 2008). We spin up P1 from its initial state for 20 years and after that we use model output from P1, at 5-day intervals, to provide the open boundary conditions for C1.

C1 shares the same topography as P1 but it has a finer vertical resolution with 165 vertical levels in total. The vertical grid thickness is 1 m near the sea surface, increases to 30 m at 410 m depth and remains at 30 m at depths further below. We spin up C1 for 5 years and use model outputs (at 5-day intervals) from the last year to construct initial and boundary fields for C2. Details of model evaluation of C1 is provided in Appendix A. The surface eddy field and the near-bottom current velocities simulated by C1 generally compare well with the observations and ECCO2 state estimate (Estimating the Circulation and Climate of the Ocean, phase 2; Figures. A1-2).

C2 has the same vertical grids as C1. We run C2 for 18 months and analyze model outputs from the last 12 months. The time-series of domain-integrated KE for C2 is provided in Appendix B. The internal lee wave generation as a result of eddy geostrophic flow impinging on small-scale topography is thought to be an important route to eddy energy dissipation (Nikurashin and Ferrari 2010b; Nikurashin et al. 2013). In order to highlight the effect of small-scale topography on eddy dissipation in the SCS, we conduct two model experiments: one includes small-scale rough topography (hereafter ROUGH) and the other does not (hereafter SMOOTH). The topography used in SMOOTH is constructed from the SRTM30_PLUS dataset by applying a spatial low-pass filter. According to the linear theory, the radiating internal lee waves have horizontal scales in the range from $|U_0/f|$ to U_0/N, which typically span wavelengths from about O(0.1) km to O(10) km (Bell 1975a, b). In order to suppress lee wave generation in the SMOOTH experiment, we chose the cutoff wavelength of the spatial low-pass filter to be 20 km which eliminates the generation of the majority of radiating lee waves. In the ROUGH experiment, synthetically-generated small-scale rough topography (See Appendix C) is added to the smoothed topography, but only in regions deeper than 500 m to avoid outcrop of the superimposed rough topography (Figure 1).

To avoid the side boundary effects, a region inside the C2 model domain is chosen for analysis (white dashed box in Figure 1), and this region is further divided into three sub-regions according to the water depth: shelf (shallower than 500 m), slope (500-3000 m) and basin (deeper than 3000 m). In addition, since the aim of this study is to investigate the role of small-scale bottom topography in dissipating eddy energy, we focus our analysis primarily on energy dissipation below the surface boundary layer (SBL), i.e., below 300 m depth.

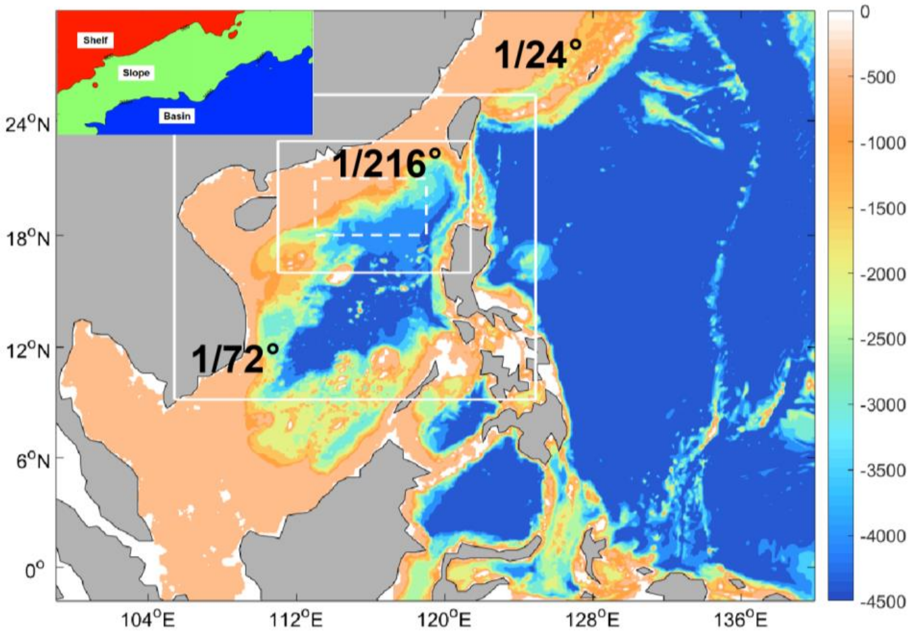

Figure 1. Bathymetry (m) used in P1 simulation (Δx = 1/24°). The boundaries of the successive nested model domains of C1 (Δx = 1/72°) and C2 (Δx = 1/216°) are delineated by white solid lines. The white dashed line inside C2 indicates the region selected for analysis (Section 3). The upper left inset marks the three sub-regions: shelf (<500 m; red), slope (500-3000 m; green) and basin (>3000 m; blue).

2.2. Energy dissipation

Away from the SBL, the kinetic energy (KE) dissipation (ε) is achieved mainly through the interior viscous dissipation expressed as:

$$\varepsilon_i = \rho A_h\left[\left(\frac{\partial \mathbf{u}_h}{\partial x}\right)^2 + \left(\frac{\partial \mathbf{u}_h}{\partial y}\right)^2\right] + \rho A_{4h}\left(\nabla_h{}^2\mathbf{u}_h\right)^2 + \rho A_z\left(\frac{\partial \mathbf{u}_h}{\partial z}\right)^2, \tag{1}$$

and the bottom drag as,

$$\varepsilon_b = \rho C_d \left|\mathbf{u}_b\right|^3, \tag{2}$$

where $\mathbf{u}_h$ is the horizontal velocity vector, A_h is the harmonic horizontal viscosity, A_{4h} is the bi-harmonic horizontal viscosity, A_z is the vertical viscosity, C_d is the quadratic drag coefficient set to be 0.0021, and $\mathbf{u}_b$ is the horizontal velocity in the bottom layer.

The loss of available potential energy (APE) via irreversible mixing is calculated as:

$$\phi = \rho\frac{K_{4h}\left(\nabla_h{}^2 b\right)^2}{N^2} + \rho\frac{K_z}{N^2}\left(\frac{\partial b}{\partial z}\right)^2, \tag{3}$$

where $b = -g(\rho - \rho_0)/\rho_0$ is buoyancy (g is gravitational acceleration, ρ is the potential density and ρ_0 is the reference density), K_{4h} is the bi-harmonic horizontal diffusivity and K_z is the vertical diffusivity.

2.3. Decomposition of ocean current into mean and eddy components

In this study, $\mathbf{u}_h$ is decomposed into the mean flow $\overline{\mathbf{u}}_h$ (including standing eddies) and eddy components $\mathbf{u}'_h$, where overbar denotes a 12-month temporal average and prime denotes deviations thereof. In this decomposition eddy motions include seasonal variability, which is, however, expected to be small since our region for analysis is well below the seasonal thermocline. Energy dissipation associated with the mean flow and eddies is then computed using Eqs. (1) and (2) with $\overline{\mathbf{u}}_h$ and $\mathbf{u}'_h$, respectively.

2.4 Decomposition of ocean current into wave and nonwave components

The internal lee waves are stationary waves in the Eulerian frame of reference. In order to isolate the wave motion, we apply a Lagrangian filter method, with the wave component defined as motions with Lagrangian frequencies exceeding the local inertial frequency (Nagai et al. 2015; Shakespeare and Hogg 2017; Yang et al. 2021). A detailed description of the Lagrangian filter method can be found in Appendix D.

Wave and nonwave energy dissipation are finally computed using Eqs. (1) and (2) with $\mathbf{u}_w$ (high-frequency velocity associated with wave motions) and $\mathbf{u}_{nw}$ (low-frequency velocity associated with nonwave motions), respectively.

2.5. Cross-scale eddy kinetic energy flux

The energy fluxes across different spatial scales are computed using a coarse-graining approach which employs convoluted filters, following Eyink and Aluie (2009). The filter-based approach is suitable for small-scale inhomogeneous flows, such as the interaction between mesoscale eddies and gravity waves (Aluie et al., 2018), unlike conventional spectral methods (e.g., Arbic et al., 2013; Capet et al., 2008).

The cross-scale energy flux can be diagnosed as follows [see Aluie et al., 2018 for details]

$$\Pi(\ell) = \Pi_h(\ell) + \Pi_z(\ell), \tag{4}$$

where

$$\Pi_h(\ell) = -\left[\left(\overline{u^2}-\bar{u}^2\right)\bar{u}_x + \left(\overline{uv}-\bar{u}\bar{v}\right)\left(\bar{u}_y+\bar{v}_x\right) + \left(\overline{v^2}-\bar{v}^2\right)\bar{v}_y\right], \text{ and} \tag{5}$$

$$\Pi_z(\ell) = -\left[\left(\overline{vw}-\bar{v}\bar{w}\right)\bar{v}_z + \left(\overline{uw}-\bar{u}\bar{w}\right)\bar{u}_z\right]. \tag{6}$$

The overbar in Eqs. (5) and (6) represents a low-pass filtered value with a cutoff scale of ℓ. Positive $\Pi(\ell)$ indicates a downscale energy transfer while negative $\Pi(\ell)$ indicates an upscale energy transfer. We compute $\Pi(\ell)$ using the following length scales ℓ=3, 5, 10, 15, 20, 27, 35, 50, 70 km in a case study of the ROUGH experiment (section 3.3).

2.6. Mean-to-wave conversion and wave energy sink

The energy exchange between the mean flow and wave motions, i.e., mean-to-wave (MTW) conversion, can be calculated as (Shakespeare and Hogg

2017):

$$\text{MTW} = \underbrace{-w_w \mathbf{u}_w \cdot \frac{\partial \mathbf{u}_{nw}}{\partial z}}_{\text{(i)vert.shear}} \underbrace{- b_w \mathbf{u}_w \cdot \frac{\nabla_h b_{nw}}{N^2}}_{\text{(ii)potential}} \underbrace{- u_w{}^2 \cdot \frac{\partial u_{nw}}{\partial x} - v_w{}^2 \cdot \frac{\partial v_{nw}}{\partial y}}_{\text{(iii)hz.strain}} \underbrace{- u_w v_w \cdot \left(\frac{\partial v_{nw}}{\partial x} + \frac{\partial u_{nw}}{\partial y} \right)}_{\text{(iv)hz.shear}} \tag{7}$$

The four terms on the right-hand side of (7) represent energy transfers of mean energy to wave energy through (i) the mean vertical shear, (ii) horizontal buoyancy gradients of the mean flow, (iii) mean horizontal strain and (iv) mean horizontal shear, respectively. Positive MTW indicates energy transfer from the mean flow to the wave field.

The wave energy sink due to viscous dissipation and irreversible mixing can be written as:

$$D = \underbrace{\left\langle A_h \left[\left(\frac{\partial \mathbf{u}_w}{\partial x} \right)^2 + \left(\frac{\partial \mathbf{u}_w}{\partial y} \right)^2 \right] + A_{4h} \left(\nabla_h{}^2 \mathbf{u}_w \right)^2 \right\rangle}_{\text{(i)hz.viscousdissipation}} + \underbrace{\left\langle A_z \left(\frac{\partial \mathbf{u}_w}{\partial z} \right)^2 \right\rangle}_{\text{(ii)vert.viscousdissipation}} + \underbrace{\left\langle \frac{K_{4h}}{N^2} \left(\nabla_h{}^2 b_w \right)^2 + \frac{K_z}{N^2} \left(\frac{\partial b_w}{\partial z} \right)^2 \right\rangle}_{\text{(iii)potentialdissipation}} \tag{8}$$

The first and second terms on the right-hand side of (8) represent wave KE dissipation by horizontal and vertical viscous effects, respectively, and the last term represents wave potential energy dissipation by mixing.

3. Result

3.1. Viscous KE dissipation

Table 1 shows the volume-integrated (below 300 m depth) KE dissipation averaged over the last 12 months of the SMOOTH and ROUGH experiments. In both experiments, large KE dissipation is mainly concentrated in the slope region. This result is consistent with recent studies that have highlighted the importance of the western continental slope in dissipating the energy of westward-propagating ocean eddies (Zhai et al. 2010; Yang et al. 2021). Compared to SMOOTH, the addition of small-scale topography in ROUGH results in a significant increase in the strength of interior viscous energy dissipation (ε_i) by 73% while a reduction in bottom frictional energy dissipation (ε_b) by 33%. Together, this leads to an overall increase of energy dissipation of 14% in ROUGH compared to SMOOTH. The increase of ε_i and decrease of ε_b in ROUGH is mainly confined to the slope and basin regions, whereas the values of ε_i and ε_b in ROUGH and SMOOTH are very similar in the shelf region. In addition, the increase in ε_i in the slope and basin regions is found to be mostly associated with the eddies, with the increase of interior dissipation associated with the mean flow more than an order of magnitude smaller (Table 1). Hereafter we will focus on the total energy dissipation, with the understanding that the total dissipation is dominated by eddy energy dissipation.

Consistent with previous idealized studies (Nikurashin et al. 2013; Yang et al. 2021), results from our realistic model simulations show that the small-scale rough topography not only enhances the overall eddy energy dissipation rate but also changes the relative importance of energy dissipation by bottom frictional drag and interior viscosity. The interior viscous dissipation becomes the dominant energy dissipation process in ROUGH, whereas the bottom frictional dissipation and interior viscous dissipation are comparable in magnitude in SMOOTH. The larger ε_i in ROUGH is likely to lead to enhanced diapycnal mixing in the ocean interior, which is potentially important for water mass transformation processes in the SCS (Wang et al. 2017). Although the loss of APE via irreversible mixing is also enhanced in the ROUGH experiment, the loss of APE is more than one order of magnitude smaller than the dissipation of KE in both SMOOTH and ROUGH. Therefore, hereafter we only focus on KE dissipation.

TABLE 1. Volume-integrated (below 300 m depth) energy dissipation (W) averaged over the last 12 months of the SMOOTH (thin) and ROUGH (bold) experiments. Shelf: shallower than 500 m; Slope: 500-3000 m; Basin: deeper than 3000 m.

Dissipation ($\times 10^6$ W)	Shelf	Slope	Basin	Total
Viscous Dissipation	4.01	20.03	7.34	31.45
	4.10	**35.11**	**15.26**	**54.47**
Viscous Dissipation	0.71/3.30	2.32/17.71	1.75/5.59	4.77/26.68
(Mean/Eddy)	**0.67/3.43**	**3.34/31.77**	**1.97/13.29**	**5.98/48.49**
Bottom Drag	2.43/7.01	2.45/12.88	4.88/9.55	9.76/29.44
(Mean/Eddy)	**1.81/6.74**	**1.78/9.45**	**3.59/2.99**	**7.18/19.18**
Loss of APE	0.40	1.08	0.04	1.53
	0.41	**2.02**	**0.07**	**2.51**

To further investigate the vertical structure of changes of energy dissipation, we composite ε_i in the two experiments based on the water depth (Figure 2). In the SMOOTH experiment, large ε_i is found mainly in the upper 1000 m due to the large velocity shear associated with the surface intensified eddy velocity structure. There is also a very narrow band of elevated ε_i very close to the smooth bottom topography which may result from the nonpropagating form drag effect (Klymak 2018; Klymak et al. 2021). In the ROUGH experiment, the band of large ε_i near the bottom becomes noticeably more enhanced as well as much wider – it is a few hundred meters thick (comparable to the root mean square height of the topography) along and above the rough topography (Figure 2f). The difference in ε_i near the bottom between SMOOTH and ROUGH can be as large as a factor of 5 in the slope and basin regions where the small-scale topography is added (Figure 2i), which, to a large extent, explains the ε_i differences between the two experiments seen in Table 1. The increase in ε_i near the bottom is mainly associated with the eddies, although the mean flow energy dissipation is also somewhat enhanced in ROUGH (Figures 2a, b, d, e).

There are also ε_i differences further up in the water column (Figures 2g, h, i), suggesting that the presence of small-scale rough topography may have an impact on upper ocean dynamics. Figure 3 shows the composition of KE as a function of water depth. Although KE in the ROUGH experiment is weaker near the bottom compared to SMOOTH, its KE is greater in the upper ocean. A similar difference is also found in eddy kinetic energy between the two experiments (not shown). A possible explanation for this result is that as eddies are dissipated more quickly in ROUGH, the eddy barotropization effect is suppressed and the baroclinicity of the along-slope flow increases, which results in stronger upper ocean currents and transport (Klymak et al. 2021).

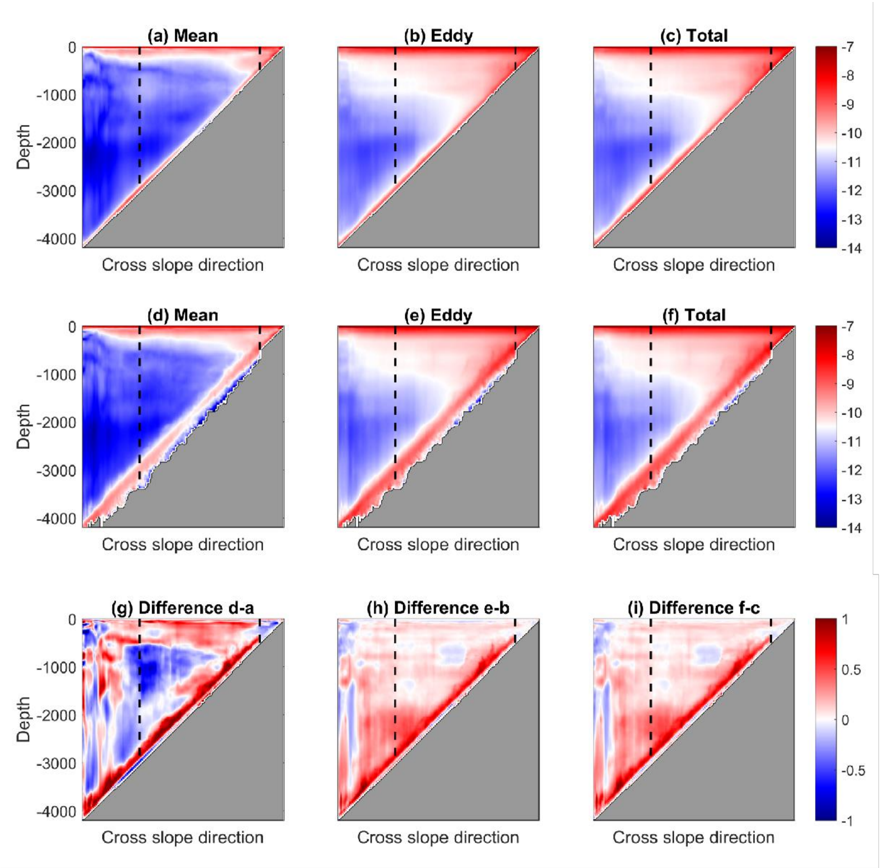

Figure 2. Composite energy dissipation rates as a function of water depth in (a-c) SMOOTH and (d-f) ROUGH (W/kg; in log10). (g-i) Differences between ROUGH

and SMOOTH (in log10). The black dash lines delineate the three sub-regions: shelf (<500 m), slope (500-3000 m) and basin (>3000 m).

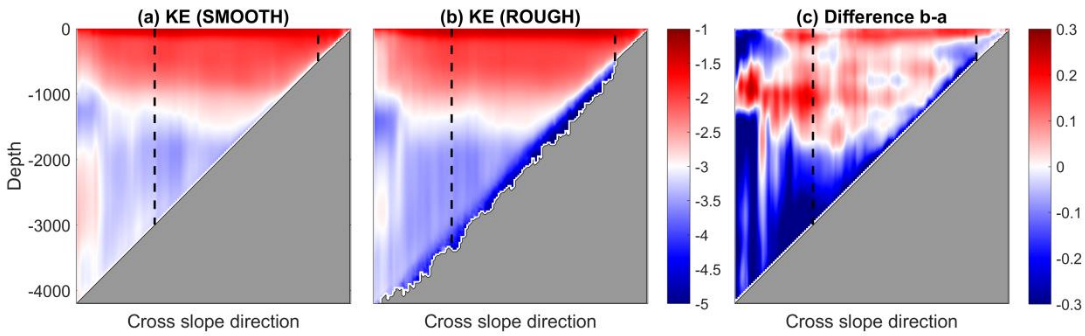

Figure 3. Composite distribution of kinetic energy as a function of water depth in (a) SMOOTH and (b) ROUGH (m^2/s^2; in log10). (c) Difference between ROUGH and SMOOTH (in log10).

Figure 4 shows wave (KE_w) and nonwave kinetic energy (KE_{nw}) in the SMOOTH and ROUGH experiments. In the SMOOTH experiment, KE_{nw} is concentrated mostly in the upper 1000 m and dominates KE (Figure 4b), with KE_w making a small contribution near the shallow end of the slope (Figure 4a). In the ROUGH experiment, KE_w is strongly enhanced in a band right above the rough topography, especially in the shallow half of the slope region (Figure 4c). Although KE_{nw} still dominates KE in most regions in ROUGH, it is of the same order of magnitude as KE_w near the rough topography (Figures 4c, d).

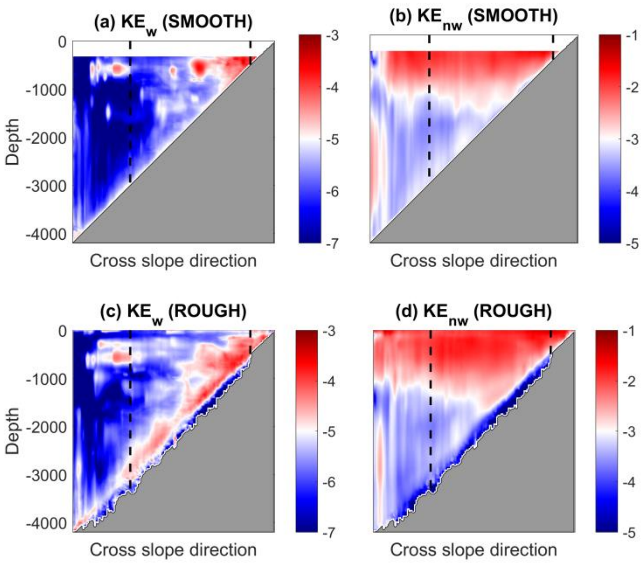

Figure 4. Composite distribution of wave and nonwave kinetic energy (m^2/s^2; in log10) as a function of water depth in (a-b) SMOOTH and (c-d) ROUGH.

The wave energy dissipation rate (ε_w) is strongly bottom-intensified in ROUGH, while in both experiments the nonwave energy dissipation rate (ε_{nw}) also shows large values in the upper ocean due to the large velocity shear there (Figure 5). The presence of small-scale rough topography in ROUGH is found to enhance both wave and nonwave energy dissipation as well as allow them to extend further upwards in the water column, whereas ε_w and ε_{nw} are more tightly confined to a narrow band immediately above the smooth topography in SMOOTH. Note that the sum of ε_w and ε_{nw} is slightly less than the total viscous dissipation (about 7% less in SMOOTH and 14% less in ROUGH), probably due to the use of a narrow 2-day filtering window (Appendix D). Table 2 shows that ε_{nw} dominates the overall energy dissipation rates in both experiments. However, with the presence of small-scale rough topography, the ratio between ε_w and ε_{nw} is almost doubled, increasing from 0.12 in SMOOTH to 0.23 in ROUGH. Below 1000 m depth, the volume-integrated ε_w is 5.73×10^6 W in ROUGH which is over 5 times larger than the 1.03×10^6 W in SMOOTH. The increase in ε_{nw} near the bottom topography is in part associated with the nonpropagating form drag (Klymak 2018; Klymak et al. 2021), an effect that we will discuss further in Section 4. Wave energy (Figure 4) and dissipation (Figure 5, Table 2) is also found in SMOOTH, particularly near the shallow end of the slope region. Here the bottom current velocity is sufficiently large (> 15 cm/s) to excite radiating internal waves.

TABLE 2. Volume-integrated (below 300 m) wave and nonwave energy dissipation (W) in the SMOOTH and ROUGH experiments.

Experiment	Wave	Nonwave	Total
SMOOTH	3.17×10^{6}	2.70×10^{7}	3.27×10^{7}
ROUGH	8.93×10^{6}	3.87×10^{7}	5.53×10^{7}

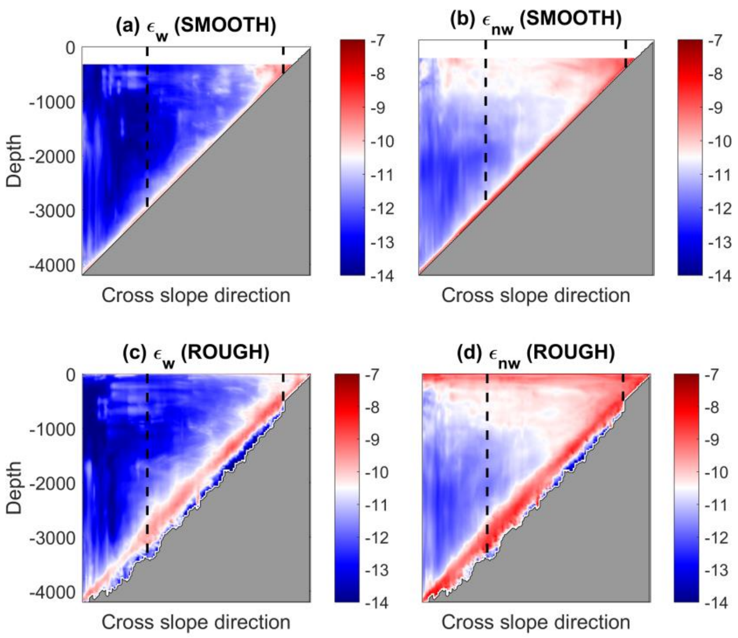

Figure 5. Composite distribution of wave and nonwave energy dissipation rates (W/kg; in log10) as a function of water depth in (a-b) SMOOTH and (c-d) ROUGH.

Recent observations (e.g., Brearley et al. 2013; Sheen et al. 2013; Waterman et al. 2013) suggest that the observed levels of energy dissipation in the bottom 1 km can be smaller by up to an order of magnitude than that implied by lee wave energy flux predicted by the linear theory. Another possible sink of lee waves generated by the rough topography is the re-absorption of lee wave energy by a vertically sheared mean flow when the flow decreases in magnitude away from the topography (Kunze and Lien 2019). Here we quantify the sinks of lee wave energy via MTW conversion and dissipation.

The MTW terms in (7) and wave dissipation terms in (8) are calculated and then averaged based on the height above the SMOOTH bottom topography (HAB, Figure 6). Terms associated with KE, e.g., viscous dissipation or MTW conversion due to velocity shear and strain, are found to dominate the lee wave energy sink in ROUGH, with terms associated with potential energy making a negligible contribution. Large values of viscous wave energy dissipation and positive MTW occur mainly below HAB = 200 m, where energy is converted from the mean flow to the lee wave field via both the mean vertical shear (green line) and mean horizontal strain (red line) terms. Above HAB = 200 m, the mean vertical shear term becomes negative, indicating re-absorption of lee wave energy by the mean flow. The sum of MTW and dissipation terms is positive in the HAB range of 0-150 m but negative above, consistent with the upward lee wave energy flux. Following the approach of Nagai et al. (2015), we average the positive and negative MTWs separately to estimate the contribution of wave re-absorption, and find that only about 5% of the lee wave energy is re-absorbed by the mean flow. This result shows that viscous dissipation is the dominant sink of lee wave energy in our ROUGH experiment, with the wave-to-mean conversion and loss of wave APE by irreversible mixing being of secondary importance.

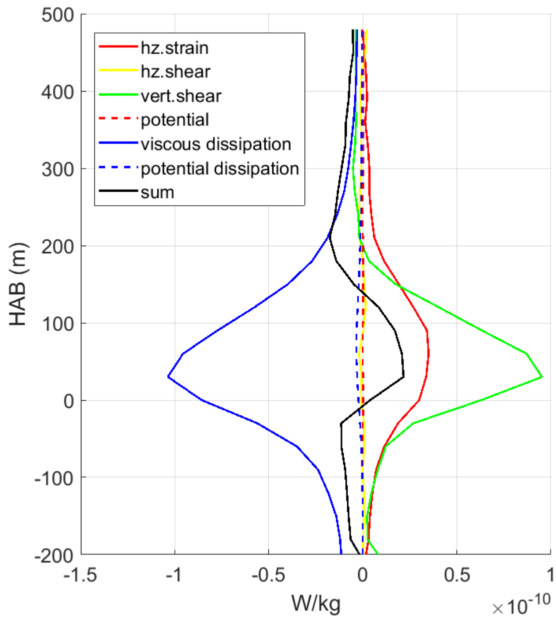

Figure 6. Average MTW and wave energy dissipation terms (W/kg). Only regions with water depth greater than 1000 m are included in the calculation.

3.2. Loss of balance

Yang et al. (2021) found in their idealized sector model experiments that the enhanced eddy kinetic energy dissipation above the rough topography is associated with greater AAI. Here we examine whether and how small-scale rough topography triggers/enhances AAI and other types of instability in the realistic model simulations of the SCS. Similar to the result of Yang et al. (2021), conditions for gravitational instability and Kelvin-Helmholtz stabilities are rarely satisfied in our model experiments. Therefore, we focus on examining the following two instability criteria and processes:

(i) sign change of $f+\xi-|S|<0$, where ξ is the relative vorticity and $S=\sqrt{\left(\frac{\partial u}{\partial x}-\frac{\partial v}{\partial y}\right)^2+\left(\frac{\partial v}{\partial x}+\frac{\partial u}{\partial y}\right)^2}$ is the horizontal strain rate (Molemaker et al. 2005; anticyclonic-ageostrophic instability or AAI).

(ii) Ertel potential vorticity (PV) takes the opposite sign of the planetary vorticity (Hoskins 1974). In the Northern Hemisphere, that means negative PV, i.e.,

$$\mathrm{PV} = \underbrace{(\nabla \times \mathrm{u})_H \cdot \nabla_H b}_{\mathrm{PV}_H} + \underbrace{(f + \xi)\frac{\partial b}{\partial z}}_{\mathrm{PV}_Z} < 0 .$$

Symmetric instability (SI) arises when the horizontal component PV_H is responsible for the negative PV and inertial instability (INI) arises when the vertical component PV_Z is responsible for the negative PV. A hybrid SI/INI develops when both PV_H and PV_Z are negative.

In both criteria, stable stratification is assumed. Table 3 shows the mean probabilities of occurrence (in percentage) of instabilities below the upper 300 m. AAI is clearly the leading instability process in both the SMOOTH and ROUGH experiments. On the other hand, high probabilities of AAI in the SMOOTH experiment are mainly concentrated at the shallow end of the slope (Figure 7a) whereas AAI in the ROUGH experiment exhibits strong near-bottom enhancement almost along the entire slope and in a pattern similar to that of ε_i (Figure 7b). The local probability of AAI near the bottom can be more than 10%, much higher than the domain-averaged probability shown in Table 3. The differences in AAI between the two experiments are mostly concentrated near the bottom which can be as large as 3% (Figure 7c). In addition to the bottom-enhanced probability of AAI, the probability of occurrence of AAI in both experiments is also elevated near the surface (Figures 7a, b) which is associated with the sharp frontal structure in winter (not shown; Barkan et al. 2015).

The presence of small-scale rough topography also leads to an increase in probabilities of INI and SI/INI in ROUGH, particularly near the bottom in the upper half of the slope region (Figures 7d-f), however, they are an order of magnitude smaller than the probability of AAI (Table 3). The higher INI and SI/INI probabilities in ROUGH may be associated with the larger near-bottom velocity shear as a result of the weakened bottom flow (Figure 3). In addition, there is little increase in the probability of SI in ROUGH compared to SMOOTH (Table 3). According to the regime diagram of Wenegrat et al. (2018), the slope Burger number ($B = N_b \tan\theta / f$, where N_b is the bottom stratification and θ is the slope angle) provides an indicator of whether the instability will be INI (B >1) or SI (B <1). In our study, N_b is about 7×10^{-3}

s^{-1}, θ is about 0.02 and f is about 5×10^{-5} s^{-1}, so the slope Burger number is about 3 which suggests that SI is only of secondary importance in our model experiments.

TABLE 3. Mean probabilities of occurrence (in percentage) of instabilities below 300 m. AAI: anticyclonic-ageostrophic instability; SI: symmetric instability; INI: inertial instability; SI/INI: hybrid symmetric and inertial instability.

Experiments	AAI	SI	INI	SI/INI
SMOOTH	0.25	0.0019	0.0067	0.0257
ROUGH	0.43	0.0023	0.0124	0.0461

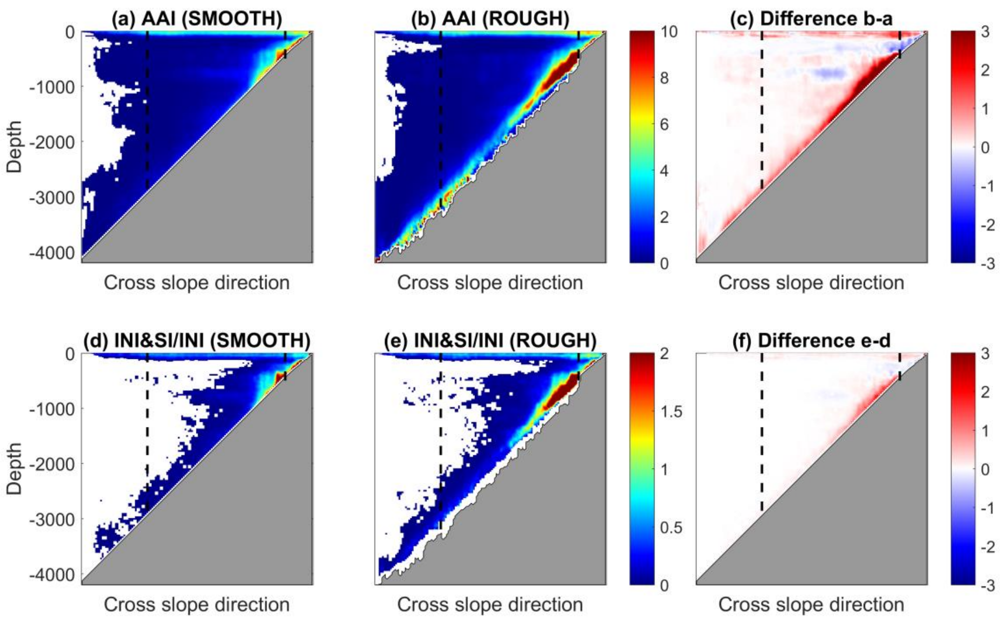

Figure 7. Probability of occurrence of instabilities and their differences between the two experiments (in percentage). (a-c) AAI; (d-f) INI and hybrid SI & INI. White areas in (a), (b), (d) and (e) indicate no instabilities.

3.3. Case study

In this section, we will further investigate the effect of small-scale topography on eddy dissipation through a case study. In the last three months (April-June) of the ROUGH simulation, a cyclonic eddy (CE) moves southwestward along the slope with its amplitude gradually decaying with time (Figure 8). On May 8th, a smaller anticyclonic eddy (AE1) is generated to the north of the CE which also propagates southwestward along the slope while at the same time interacting with the CE. On June 8th, another anticyclonic eddy (AE2) emerges on the southeast side of the CE and begins to interact with the CE. During the interaction of the eddy pairs, two strong jets form between the coupled, counterrotating eddies. Here we select a 200 km long section along the 2000-m isoline to present our analysis of the case study (yellow line in Figure 8). Figure 9 shows the temporal evolution of the section-mean energy dissipation rate. Consistent with the composite result of Figure 3f, large energy dissipation rates (ε_i) are concentrated in the bottom 500 m which is one or two orders of magnitude larger than that in the interior. Further, the bottom dissipation is particularly enhanced when the selected section lies between these eddy pairs (i.e., May 23rd and June 8th).

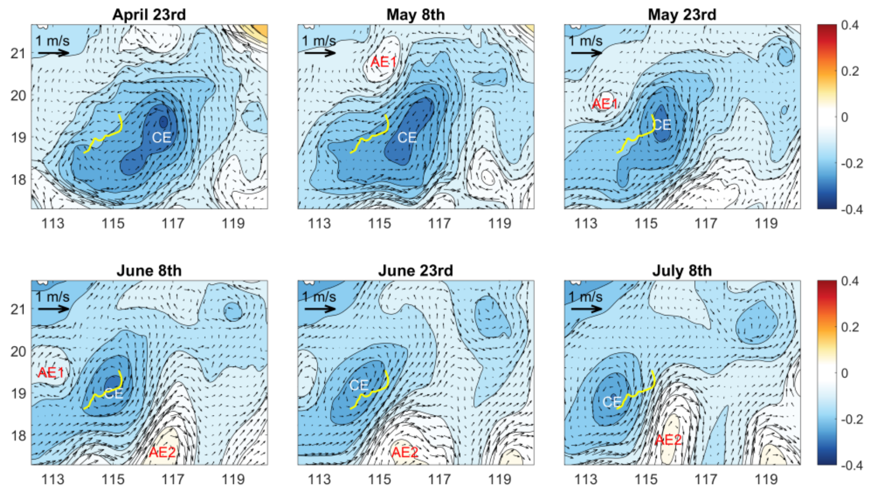

Figure 8. Maps of sea surface height (shading with an interval of 0.05 m) and surface velocities (arrows) from April 23rd to July 8th in ROUGH. The yellow line indicates the 200-km long section along the 2000-m isoline which is selected for further

analysis. Locations of the cyclonic eddy and two anticyclonic eddies are marked by "CE", "AE1" and "AE2", respectively.

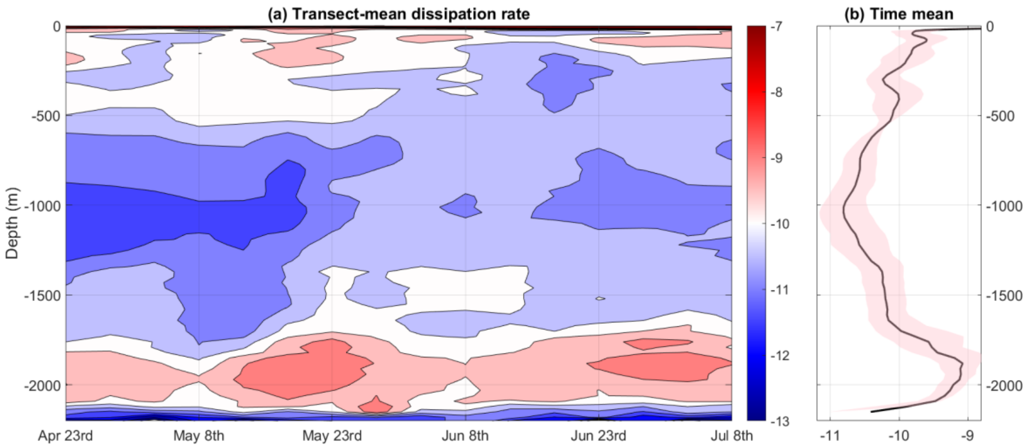

Figure 9. (a) Time evolution of section-mean dissipation rate (W/kg; in log10). (b) Time- and section-mean dissipation rate (black line; W/kg; in log10). The color shading in (b) represents one standard deviation.

We focus on May 23rd when the bottom-enhanced ε_i becomes elevated (Figure 9). On May 23rd, the section lies between the AE1 and CE, closer to the CE (Figure 8). Large near-bottom along-slope currents with speed over 0.1 m/s can be found along the section (Figures 10c, d). As a result of strong eddy flow impinging on the small-scale topography on the slope, lee waves are generated which are visible in the vertical velocity field whose phase lines tilt against the mean flow, as predicted by the linear lee wave theory (Figure 10a). The bottom topography is less rough towards the northeast end of the section (160-190 km), and the waves generated there, being near the linear limit, do not decay significantly with height which results in smaller ε_i (Figure 10b). Figure 10e shows there are patches of negative A-$|S|$, conditions favorable for the occurrence of AAI, right above the rough topography, which correspond well with areas of enhanced ε_i (Figure 10b). Our case study therefore suggests that the presence of small-scale topography enhances near-bottom eddy energy dissipation via triggering AAI. AAI can arise through a shear-assisted resonance of at least one unbalanced wave with coincident Doppler-shifted phase speeds (McWilliams et al. 2004), and wave-wave interaction provides a mechanism of direct energy transfer toward small scales, without a turbulent cascade process, thus enhancing the viscous dissipation (Staquet and Sommeria 2002).

Recent studies found that submesoscale instabilities such as SI or INI may develop when the abyssal boundary currents flow in the direction of Kelvin wave propagation (e.g., Wenegrat et al. 2018; Naveira Garabato et al. 2019). The underlying mechanism involves a down-slope flow induced by topographic frictional stress acting on an abyssal boundary current which tilts isopycnals toward the vertical and compresses them horizontally. When the lateral stratification and shear become sufficiently large, PV changes sign and SI and/or INI may develop. At our selected section, the along-slope near-bottom current flows southwestward, i.e., in the direction of Kelvin wave propagation, and there are indeed patches of negative PV close to the rough topography (Figure 10f). It is further found that both the horizontal component PV_H and vertical component PV_Z are negative in most areas of negative PV (not shown), suggesting that the instability type is hybrid SI/INI. Note that there are overlaps between areas of negative PV and areas of AAI, because negative absolute vorticity fulfills the instability criterion for both INI and AAI.

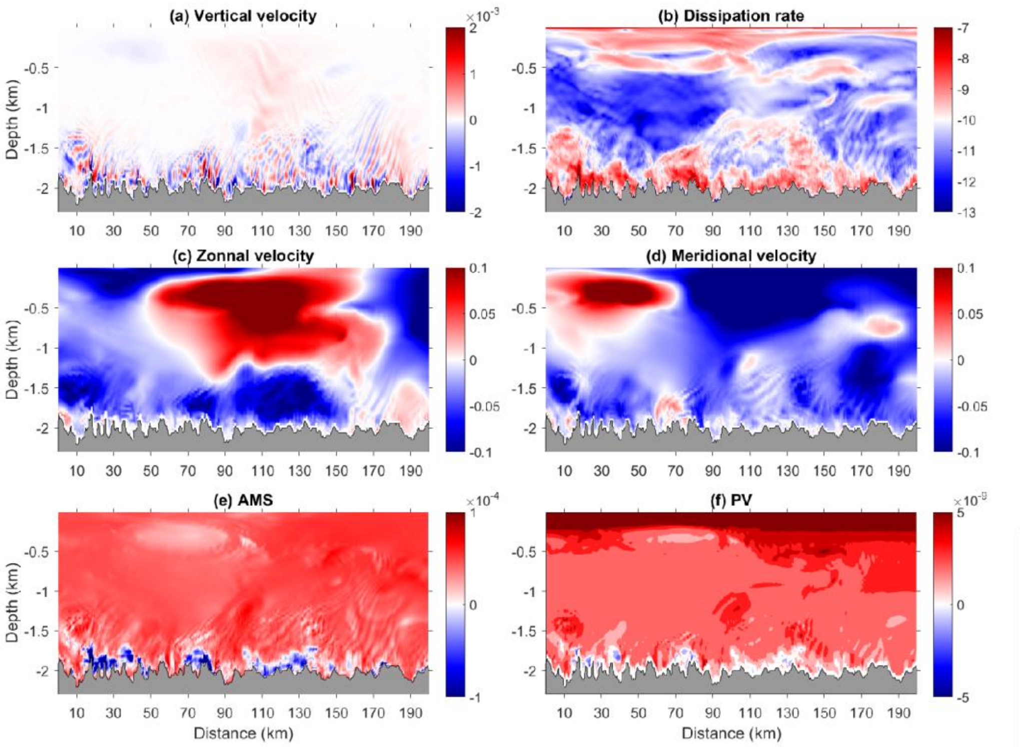

Figure 10. (a) Vertical velocity (m/s); (b) dissipation rate (W/kg); (c) zonal velocity (m/s); (d) meridional velocity (m/s); (e) absolute vorticity minus the horizontal strain rate (s^{-1}) and (f) potential vorticity (s^{-3}) along the selected section on May 23rd.

Figure 11 shows wave and nonwave velocities and energy dissipation rates of the case study. The nonwave velocity $\mathbf{u}_{nw}$ dominates and is generally surface intensified, while the wave velocity $\mathbf{u}_{w}$ is weaker with a magnitude of a few cm/s and is mainly concentrated above the rough topography (Figures 11a, b, e). Both ε_w and ε_{nw} are bottom-enhanced with comparable magnitudes, while large values of ε_{nw} are also present in the upper ocean associated with large velocity shear there. On a closer look, the bottom-enhanced ε_{nw} appears to be confined closer to the seafloor than ε_w (Figures 11c-f), which is consistent with the fact that lee waves generated via flow-topography interaction radiate away from the topography and as a result dissipate further higher up in the water column.

Figure 10c shows that the zonal flow along the selected section is strongly baroclinic, trending to zero at around 1200 m depth. It's interesting to note that the wave amplitudes attenuate at around 1500 to 1000 m depth (Figure 11a), which points to the possibilities of (1) wave-to-mean conversion sapping energy from the waves and (2) inertial/critical level effects driving dissipation as the horizontal flow speed reduces with height and the intrinsic wave frequency drops towards the inertial (Kunze and Lien 2019).

Figure 12 shows the MTW and wave energy dissipation for the case study. The MTW is patchy but is on average positive in the bottom 300 m, indicating energy transfer from the mean flow to lee waves. At around 1500 to 1200 m depth where the lee waves attenuate, more patches of negative MTW can be spotted and the mean MTW term also shifts to negative (Figure 12c). At 1500 m depth, the mean MTW term is about one order of magnitude larger than wave dissipation, indicating that re-absorption of lee wave energy by the mean flow is the leading route for wave energy loss at that depth. The negative MTW is mainly caused by the mean vertical shear term (Figures 12b, c), consistent with the mechanism discussed by Kunze and Lien (2019). Integrated over the whole water column, we find that about 10-15%[2] of the lee wave energy is re-absorbed by the mean flow in this case study, while the rest is dissipated via viscous processes.

---

[2] The internal-wave energy fluxes are horizontally averaged over some typical wavelength before estimating the contribution of wave re-absorption. Using different horizontal scales (5-10 km) only leads to small changes (10-15%) in our result.

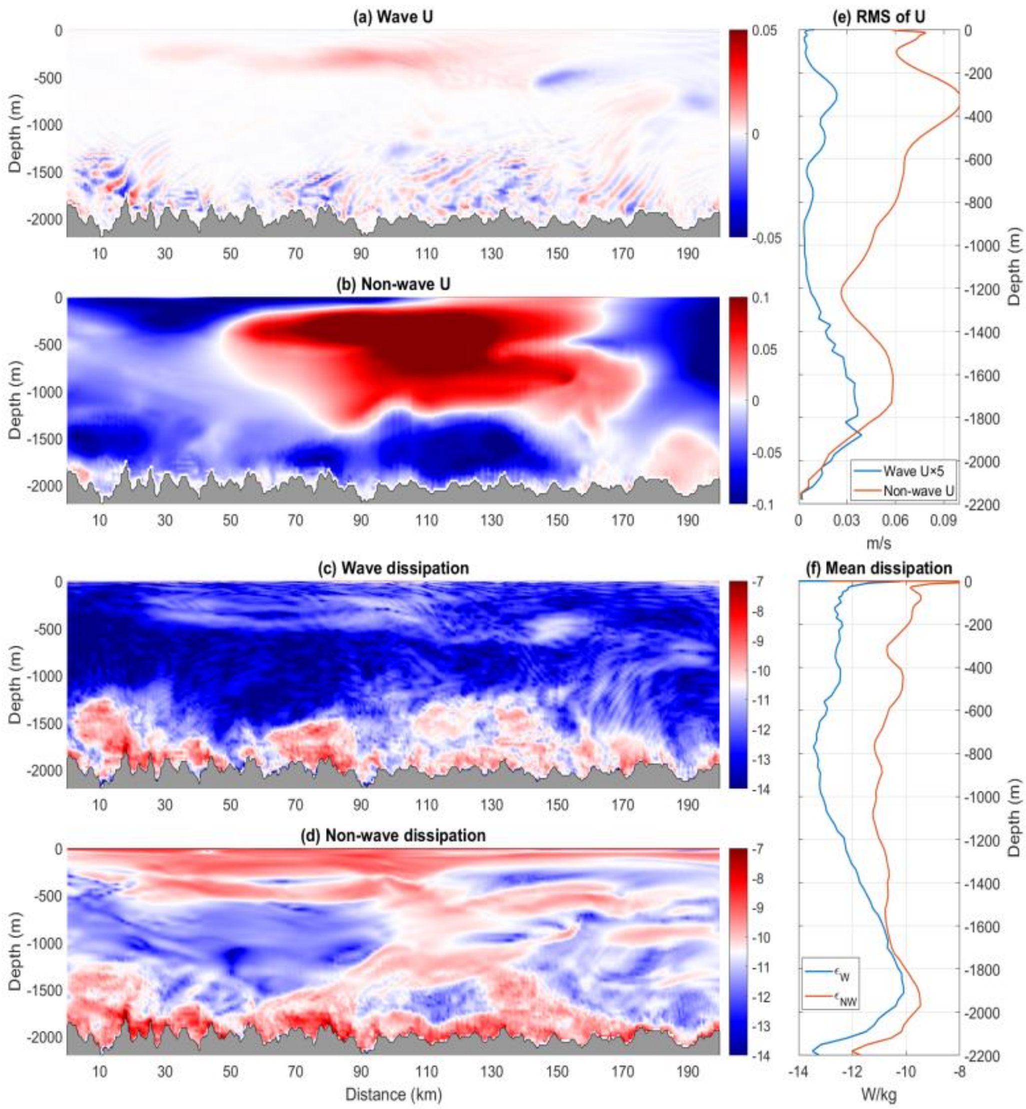

Figure 11. Wave and nonwave velocities (m/s) and dissipation rates (W/kg; in log10) of the case study. The root mean square (RMS) of velocities (m/s) and section-average dissipation rates (W/kg; in log10) are shown in the two side panels (e & f). Note that the RMS wave velocity is multiplied by a factor of 5 in panel e.

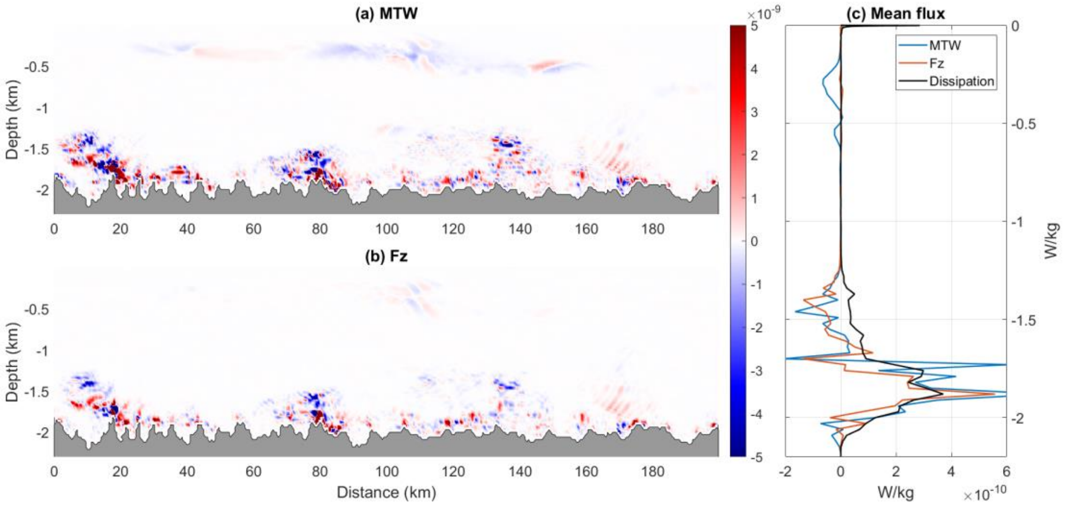

Figure 12. (a) Total mean-to-wave conversion and (b) the mean vertical shear term (W/kg) in the case study. (c) Section-average energy conversion and dissipation (W/kg). Blue line represents the total MTW term, red line represents the mean vertical shear term and black line represents the wave energy dissipation (W/kg; note the sign of dissipation is reversed).

We then compute the section-averaged cross-scale kinetic energy flux in the case study using the coarse-graining approach (Figure 13). The fluxes are directed toward larger scales (negative) for most of the investigated scales, particularly in the upper 1400 metres, which is consistent with the “inverse cascade” predicted by geostrophic turbulence theory (Salmon 1998). However, close to the rough bottom, downscale energy fluxes dominate especially at scales less than 15 km. These significant downscale energy transfers at small scales above the rough bottom highlight the important role of small-scale topography in transferring energy out of the mesoscale flow fields via instability and wave generation into small-scale motions which are subsequently dissipated. Figure 14 shows the cross-scale kinetic energy flux at scale of 3 km. Patches of downscale and upscale energy fluxes are found to concentrate right above the rough topography (Figure 14b). Regions of large downscale energy fluxes are partly compensated by large upscale energy fluxes (Figure 14a), though downscale fluxes still dominate the total fluxes. In addition, areas of large downscale energy fluxes generally coincide with areas of enhanced ε_i (Figure 10b). The compensation relationship between positive and negative energy fluxes may be associated with the re-absorption of wave energy by currents (Kunze and Lien 2019).

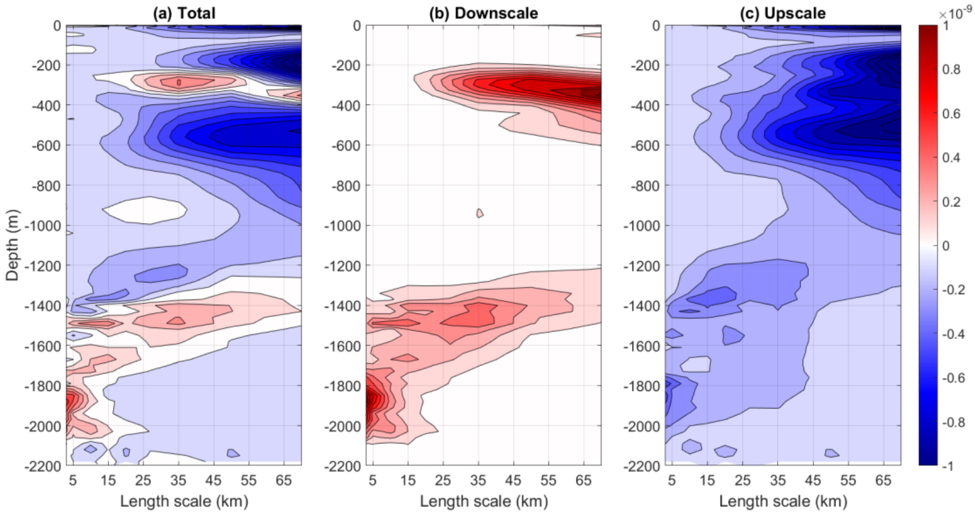

Figure 13. (a) The section-averaged cross-scale kinetic energy flux (W/km) in the case study computed with the coarse-graining approach and its (b) downscale and (c) upscale contributions. The downscale and upscale energy fluxes are computed by setting the negative and positive fluxes, respectively, to zero before spatially averaging and adding up to the total flux.

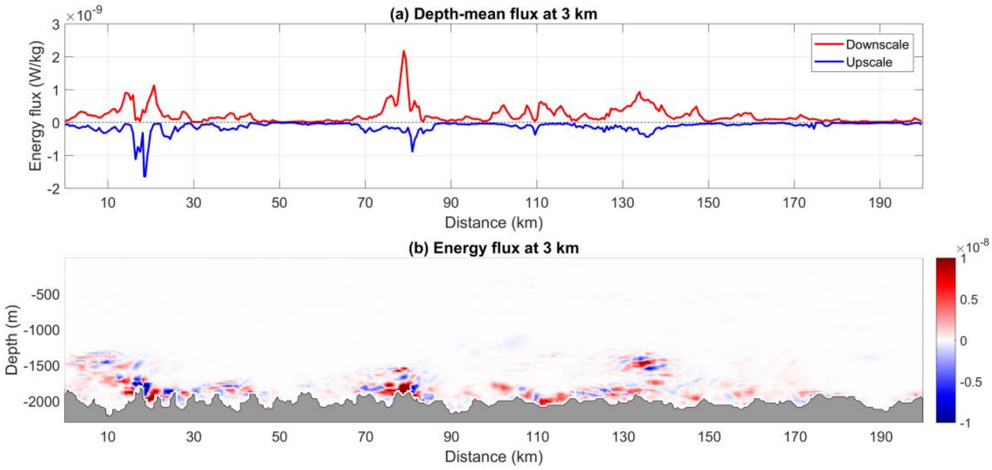

Figure 14. (a) Depth-mean cross-scale kinetic energy flux (W/km) at the scale of 3 km. (b) Cross-scale kinetic energy flux (W/km) at the scale of 3 km along the selected section on May 23rd.

4. Discussion

a. Nonpropagating form drag

Compared to the SMOOTH experiment, our result shows that the presence of small-scale rough topography increases the interior energy dissipation rate in the ROUGH experiment by 73% (Table 1). Among this increase, one third can be explained by the enhanced wave energy dissipation ε_w, and the remaining two thirds is due to an increase in nonwave energy dissipation ε_{nw} (Table 2). The nonpropagating form drag effect may contribute to this increase in ε_{nw} (Klymak 2018; Klymak et al. 2021). For medium-scale and large-amplitude topography or weak near-bottom flow that are characterized by $U_0k/f<1$ and $Nh/U_0>>1$ (k is the horizontal topographic wavenumber and h is the root mean squared topographic height), the flow is inherently nonlinear and dissipative, and that the nonpropagating form drag is likely to be more important for energy dissipation than propagating lee waves. Figure 11f shows that the bottom-enhanced ε_{nw} is indeed more closely confined to the topography than ε_w, suggesting "nonpropagating" dissipation.

Following Klymak et al. (2021), the nonpropagating drag can be parameterized as: $D_{np} = \frac{U_0^2 h}{L}\frac{\pi}{2}\left[\frac{Nh}{U_0} + \pi\right]$, where L is an along-flow lateral scale. The nonpropagating effect has a vertical blocking scale of the topography $\pi U_0 / N$ (Klymak et al. 2010) which is typically hundreds of meters. The near-bottom vertical resolution of our model is 30 m, which should be fine enough to resolve the nonpropagating drag. We take velocity and buoyancy frequency averaged over 200-400 m above the bottom as the bottom velocity ($\mathbf{u}_b$) and bottom buoyancy frequency (N_b), and calculate the nonpropagating work in the two experiments (only water depth greater than 1000 m is considered). The mean nonpropagating work is 1.0 mW/m^2 and 1.8 mW/m^2 for the SMOOTH and ROUGH experiments, respectively, indicating that the nonpropagating effect becomes more enhanced in the ROUGH experiment.

Two factors may explain the enhanced nonpropagating form drag in ROUGH: larger topography amplitude and weaker bottom flow. Although only rough topography with horizontal scales less than 20 km is added onto the background topography in ROUGH, Figure 5 shows that including these small-scale topographic features significantly weakens the near-bottom flow. When the near-bottom flow becomes sufficiently weak such that $u_0k/f<1$ and $Nh/u_0>>1$, the waves are no longer radiating and the flow is at least partially blocked by the topography. As a result, adding small-scale rough topography in ROUGH not only leads to generation of radiating lee waves but also enhances the nonpropagating drag.

We calculate the horizontally-averaged Eliassen-Palm (EP) fluxes which is the z-coordinate representation of the form stress between isopycnal layers (Eliassen 1960). The EP flux is defined as $\rho\left\langle uw-\frac{f}{N^2}vb, vw+\frac{f}{N^2}ub\right\rangle$ (angled bracket indicates a horizontal average). We further split them into wave and non-wave parts (i.e. $\rho\left\langle u_w w_w-\frac{f}{N^2}v_w b_w, v_w w_w+\frac{f}{N^2}u_w b_w\right\rangle$ and $\rho\left\langle u_{nw} w_{nw}-\frac{f}{N^2}v_{nw} b_{nw}, v_{nw} w_{nw}+\frac{f}{N^2}u_{nw} b_{nw}\right\rangle$). Figure 15 shows the horizontally-averaged EP fluxes as a function of height above bottom topography in SMOOTH and ROUGH. As expected, the wave part is very small in SMOOTH and the EP flux in this experiment is almost entirely due to non-wave motions. With the addition of rough topography, both wave and non-wave fluxes become significantly enhanced, although the EP fluxes due to non-wave motions still dominate. In both experiments, the wave and nonwave fluxes are bottom-intensified. It is worth noting that in ROUGH the wave flux peaks further away from the bottom topography than nonwave part, similar to the difference in vertical structure between wave and non-wave energy dissipation (Figure 11f).

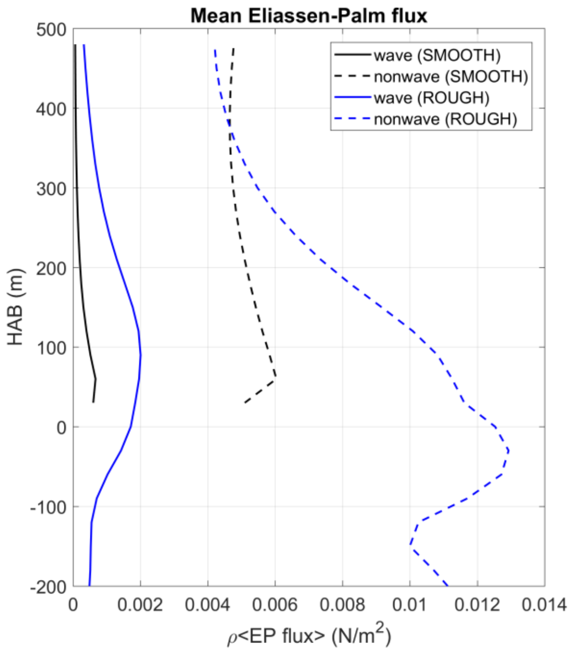

Figure 15. Horizontally-averaged EP fluxes due to wave and non-wave motions in SMOOTH and ROUGH.

b. Tides

The SCS is well known as a region with very strong tidal flows. Tides are also known to modify the generation of lee waves. For example, a recent study by Shakespeare (2020) found that the inclusion of tides can potentially suppress the energy flux into lee waves by 13%–19% as a result of interdependence of internal tide and lee wave generation. Preliminary analyses suggest that this suppression effect of tides on lee wave generation in our model is less than that reported by Shakespeare (2020), although we note the difficulty of unambiguously distinguishing the lee wave and internal tide energy in the experiment of ROUGH with tides. The effect of tides on lee wave generation and dissipation is worth further investigation but is left for a future study.

5. Summary

The effect of small-scale topography on eddy dissipation in the northern SCS is investigated in a high-resolution nested-modelling system initialized with either a smooth topography or a synthetically-generated rough topography. In both experiments, large KE dissipation is found to be mostly concentrated in the slope region, highlighting the importance of continental slope at the western boundary in dissipating westward-propagating eddies (Zhai et al. 2010; Yang et al. 2021). Consistent with previous idealized studies (Nikurashin et al. 2013; Yang et al. 2021), results from our realistic model simulations show that the small-scale rough topography not only significantly enhances the overall eddy energy dissipation rate but also changes the relative importance of energy dissipation by bottom frictional drag and interior viscosity. The bottom-enhanced viscous energy dissipation is likely to lead to elevated diapycnal mixing in the ocean interior, with important implications for water mass transformation processes in the SCS (Wang et al. 2017).

The role of lee wave generation in eddy energy dissipation is investigated using a Lagrangian filter method. It is found that when the small-scale rough topography is added, both wave energy and wave energy dissipation rate are strongly enhanced in a band right above the rough topography. About one-third of the increase in energy dissipation in the rough topography experiment can be explained by the enhanced wave energy dissipation, with the remaining two-thirds due to an increase in nonwave energy dissipation. The addition of small-scale topography increases the amplitude of bottom topography and weakens the near-bottom flow and as a result some waves generated are no longer radiating and the flow becomes at least partially blocked by the topography. Our results show that the nonpropagating work is almost doubled when small-scale rough topography is added, suggesting that the increased nonpropagating form drag contributes to the enhanced nonwave energy dissipation.

Similar to Yang et al. (2021), AAI is found to be the leading instability in our model experiments. The enhanced eddy energy dissipation in experiment including small-scale rough topography is associated with greater probabilities of occurrence of AAI. Although probabilities of other types of submesoscale instabilities such as INI and hybrid SI/INI also become higher in the presence of rough topography, they are an order of magnitude smaller than the probability of AAI.

Our study provides further evidence that small-scale rough topography plays a key role in eddy energy dissipation. The magnitude and vertical structure of diapycnal mixing generated in the process of eddy-rough topography interaction is not yet well known, but have important implications for large-scale ocean circulation and climate (e.g., Saenko et al. 2012).

Acknowledgments.

ZY and ZJ are supported by National Science Foundation of China (41776006, 41822601), Taishan Scholar Funds (tsqn201909052), Qingdao applied research project. The research presented in this paper was carried out on the High Performance Computing Cluster supported by National Supercomputer Center in Tianjin. We thank two anonymous reviewers for their helpful comments that led to significant improvement of this manuscript.

Data availability statement.

All the model configuration files and codes used for analyses are available from the corresponding author upon reasonable request.

APPENDIX A

Model evaluations

The root-mean-square sea surface height (SSH) variability computed from output of the C1 model in the last model year is compared with that derived from the AVISO sea surface height anomaly data (https://www.aviso. altimetry.fr/en/my-aviso.html). The spatial pattern of the modelled SSH variability is generally comparable to that derived from AVISO data, with large amplitude of SSH variability on the northern slope of the SCS and southeast of the Vietnam coast. The observational field looks smoother than our model result which may be due to a multi-year average (1993-2016).

Bottom stratification and bottom velocity are two important parameters that determine whether the lee waves can radiate or remain trapped above topography. Here we verify the stratification and velocity profiles of C1 model with the WOA climatology data and an eddying global state estimate (i.e., the Estimating the Circulation and Climate of the Ocean, phase 2, high-resolution global-ocean and sea ice data synthesis (ECCO2) state estimate). The average buoyancy frequency (N) profiles along the 2000- and 3000-m isolines are shown in Figures A2a, b. The model results match the observed profiles reasonably well and have similar bottom stratification. Figures A2c, d show the velocity profiles from C1 model and ECCO2. The velocity profiles are again close, although our model shows weaker velocity in the upper ocean. This may be due to a lack of high-frequency atmospheric forcing used in C1. However, our study mainly focuses on the effect of bottom small-scale topography, and we think this lack of high-frequency surface forcing will not affect our main conclusions.

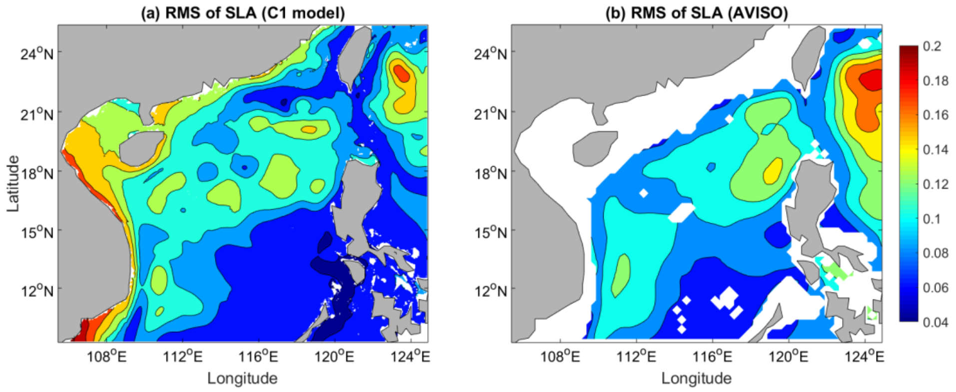

Figure A1. Root mean square sea surface height variability (m) in the South China Sea based on (a) C1 model output and (b) satellite altimeter data. Satellite data in regions shallower than 200 m have been masked out.

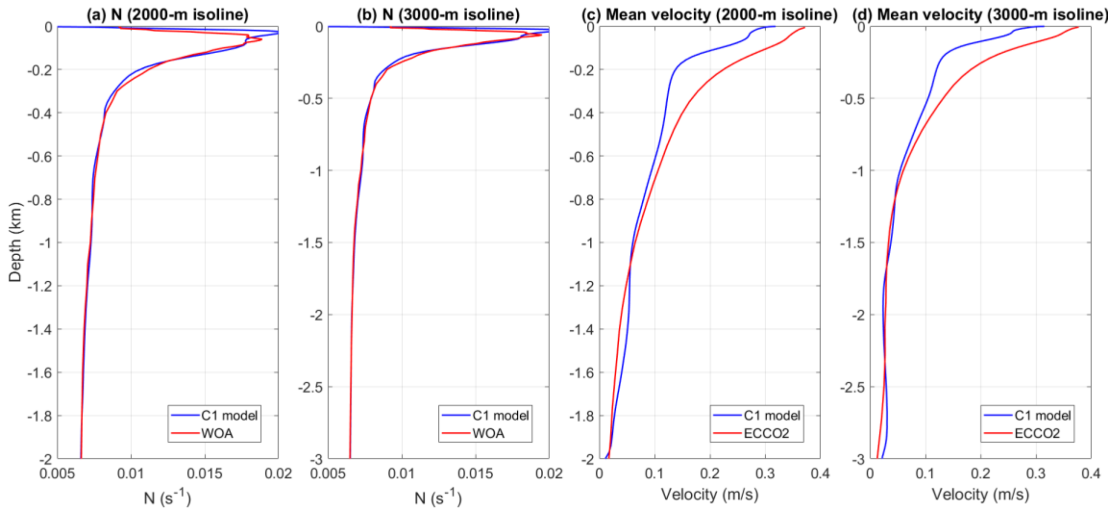

Figure A2. The average (a-b) buoyancy frequency (s^{-1}) and (c-d) velocity (m/s) profiles along the 2000- and 3000-m isolines.

APPENDIX B

Time series of domain-integrated KE

Figure B1 shows the time series of domain-integrated KE for SMOOTH and ROUGH experiments. The upper ocean KE in both experiments gradually increases in the first 6 months or so, but after that, the upper ocean KE generally reaches quasi-equilibrium and shows no obvious trend. KE in the lower ocean, which is the focus of our study, shows no obvious trend in the 12-month analysis window, either. To further quantify the KE drift in our model, we estimated the annual drift of KE by a linear regression of KE in the last 12 months. In both experiments, the KE drift is less than 3% of the total KE. Based on these results, we believe that the "eddy" part of the dissipation in our analysis is indeed associated with eddies rather than a drifting mean state.

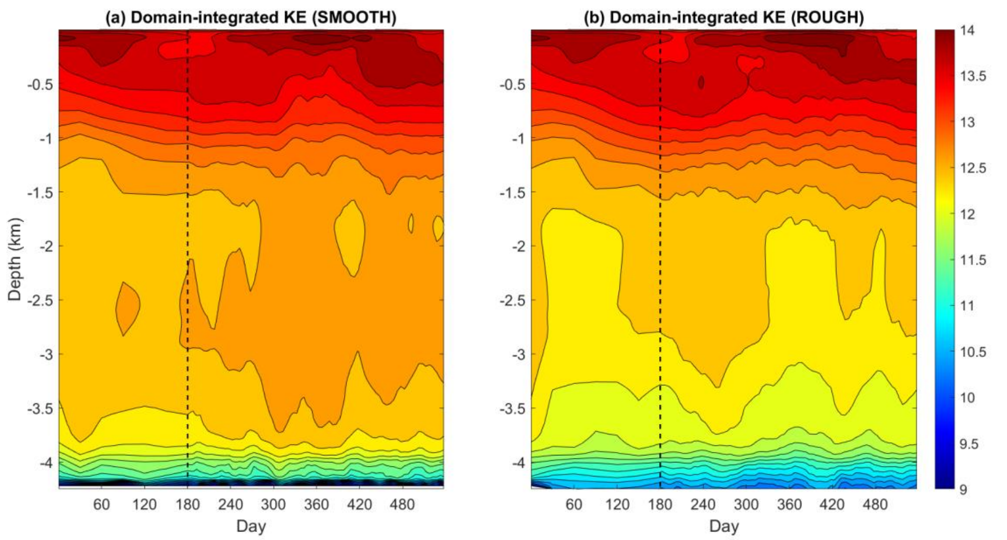

Figure B1. Time series of domain-integrated KE for (a) SMOOTH and (b) ROUGH (J; in log10).

APPENDIX C

Method for synthetically-generated rough topography

The synthetic topography is computed as a sum of Fourier modes with amplitudes given by the observed topographic spectrum of the SCS, following the stochastic seafloor model proposed by Goff and Jordan (1988). The Goff and Jordan model is a topographic spectrum model at O(0.1-100) km scales based on a statistical description of abyssal hills,

$$P(k,l)_{GJ} = \frac{2\pi h^2(\mu-2)}{k_0 l_0}\left[1+\frac{k^2}{k_0^2}\cos^2(\phi-\phi_0)+\frac{l^2}{l_0^2}\sin^2(\phi-\phi_0)\right]^{-\mu/2}, \quad \text{(C1)}$$

where (k, l) are the horizontal wavenumbers in the zonal and meridional directions, ϕ is the angle between the wave vector and the eastward direction, h^2 is the variance of the topographic height, (k_0, l_0) are the characteristic wavenumbers of the principal axes of anisotropy, ϕ_0 is the azimuthal angle, and μ is the high-wavenumber roll-off slope.

The parameters in (C1) need to be fitted from high-resolution multibeam data. However, multibeam observations in the SCS are very sparse. Here we assume for simplicity that the synthetic rough topography is isotropic ($k_0 = l_0$) and use the high-resolution single beam topography data from the U.S. National Geophysical Data Center (NGDC, https://www.ncei.noaa.gov/maps-and-geospatial-products) to estimate the spectral characteristics of small-scale topography in SCS. A total of 164 single beam data are collected (Figure C1a). Following Nikurashin and Ferrari (2011), all data from waters deeper than 500 m and with along-track resolution of at least 2 km are divided into 50 km long segments. The total number of ~3,000 segments is used. In each segment, the large-scale topographic slope is removed by fitting a straight line before computing the topographic spectrum. Spectra are binned and averaged over a 2° × 2° grid. Then synthetic topography is computed as a sum of Fourier modes with amplitudes given by the two-dimensional topographic spectrum and random phases. Figure C1b shows the synthetically-generated topography in the SCS with horizontal scales less than 20 km. Topographic roughness is enhanced near the Luzon Strait, the Xisha Islands and the Nansha Islands. The northern slope, however, is relatively smooth.

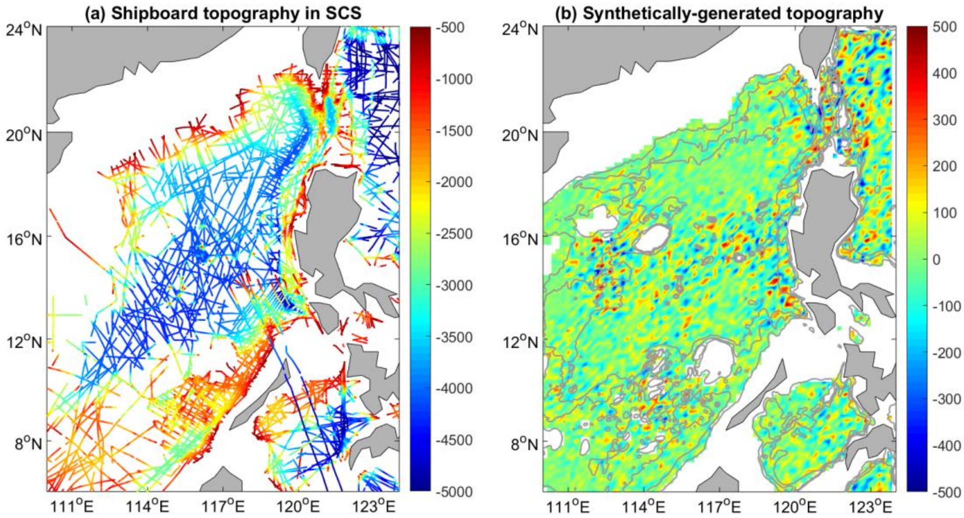

Figure C1. (a) Shipboard single beam topography data from the U.S. National Geophysical Data Center. The color shading shows the observed bathymetry (m), (b) synthetically-generated topography in the SCS with horizontal scales less than 20 km. Gray lines represent the isolines of 1000 m, 2000 m and 3000 m, respectively.

APPENDIX D

Lagrangian Filtering Method

The internal lee waves are stationary waves in the Eulerian frame of reference. In order to isolate the wave motion, we apply a Lagrangian filter method, with the wave component defined as motions with Lagrangian frequencies exceeding the local inertial frequency (Nagai et al. 2015; Shakespeare and Hogg 2017; Yang et al. 2021). The method involves the following steps:

1. Particle tracking. Nearly 150 million flow-following particles (one particle at every model grid point) are introduced in the SMOOTH and ROUGH experiments and their trajectories are computed every hour over 2-day analysis periods (May 12^{nd}-13^{rd} for SMOOTH and May 22^{nd}-23^{rd} for ROUGH). Then the paths of these particles are computed online following the model algorithm by making use of the MITgcm package for float advection. Note that only the horizontal velocities are used for particle advection (hence semi-Lagrangian).

2. Forward interpolation. Interpolate fields of interest (e.g., w and density) from the model grid to the particle locations.

3. Filtering. The wave field is isolated by applying a high-pass filter (with a cutoff frequency of local inertial frequency) to the velocity field following the particle trajectories.

4. Reverse interpolation. Interpolate the filtered fields from the scattered particle locations back to the model grid.

Here we only run the Lagrangian particle experiments for an analysis period of 2 days because of the computational challenge. To evaluate the ringing effect on our filtered results, we run another Lagrangian particle experiment in ROUGH for a longer analysis time period of 6 days. Figure D1 shows the results of wave and nonwave energy dissipation from Lagrangian experiments with 2-day and 6-day analysis periods. The two different analysis periods produce similar bottom-enhanced dissipation patterns. Quantitatively, the volume-integrated wave dissipation below 300 m is 7.24×10^6 W for 2-day analysis period and 7.88×10^6 W for 6-day analysis period, representing an increase of about 8%. However, this difference is much less than the magnitude of temporal variations of wave dissipation.

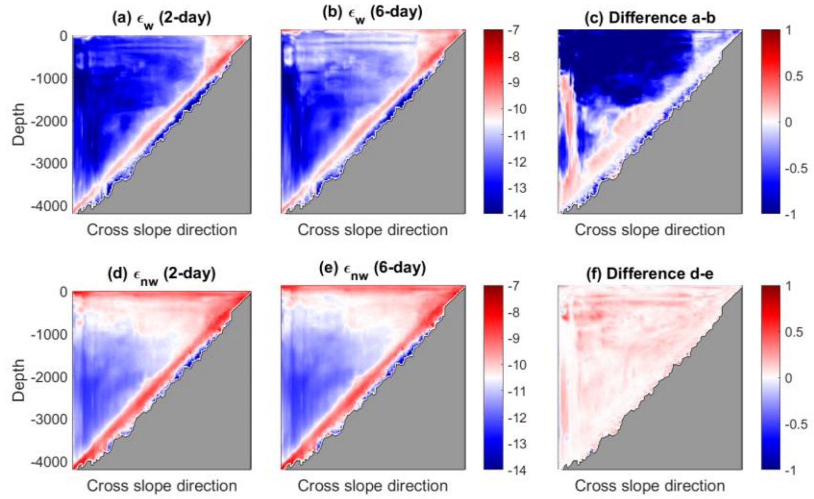

Figure D1. Composite distribution of wave (a-c) and nonwave energy (d-f) dissipation with different analysis periods (in log 10).

REFERENCES

Alford, M. H., A. Y. Shcherbina, and M. C. Gregg, 2013: Observations of near-inertial gravity waves radiating from a frontal jet. J. Phys. Oceanogr., 43, 1225–1239, https://doi.org/10.1175/JPO-D-12-0146.1.

Aluie, H., M. Hecht, and G. K. Vallis, 2018: Mapping the energy cascade in the North Atlantic Ocean: The coarse-graining approach. J. Phys. Oceanogr., https://doi.org/10.1175/JPO-D-17-0100.1.

Arbic, B. K., and Coauthors, 2009: Estimates of bottom flows and bottom boundary layer dissipation of the oceanic general circulation from global high-resolution models. J. Geophys. Res., 114, C02024, https://doi.org/10.1029/2008JC005072.

Arbic, B. K., K. L. Polzin, R. B. Scott, J. G. Richman, and J. F. Shriver, 2013: On eddy viscosity, energy cascades, and the horizontal resolution of gridded satellite altimeter products. J. Phys. Oceanogr., https://doi.org/10.1175/JPO-D-11-0240.1.

Barkan, R., K. B. Winters, and S. G. Llewellyn Smith, 2015: Energy cascades and loss of balance in a reentrant channel forced by wind stress and buoyancy fluxes. J. Phys. Oceanogr., https://doi.org/10.1175/JPO-D-14-0068.1.

Becker, J. J., and Coauthors, 2009: Global Bathymetry and Elevation Data at 30 Arc Seconds Resolution: SRTM30_PLUS. Mar. Geod., 32(4), 355–371. https://doi.org/10.1080/01490410903297766.

Bell, T., 1975a: Lee waves in stratified flows with simple harmonic time dependence. J. Fluid Mech., 67, 705–722, https://doi.org/10.1017/S0022112075000560.

——, 1975b: Topographically generated internal waves in the open ocean. J. Geophys. Res., 80, 320–327, https://doi.org/10.1029/JC080i003p00320.

Brearley, J. A., K. L. Sheen, A. C. Naveira Garabato, D. A. Smeed,and S. Waterman, 2013: Eddy-induced modulation of turbulent dissipation over rough topography in the Southern Ocean. J. Phys. Oceanogr., https://doi.org/10.1175/JPO-D-12-0222.1.

Capet, X., J. C. McWilliams, M. J. Molemaker, and A. F. Shchepetkin, 2008: Mesoscale to submesoscale transition in the California current system. Part III: Energy balance and flux. J. Phys. Oceanogr., https://doi.org/10.1175/2008JPO3810.1.

Carton, J. A., and B. S. Giese, 2008: A reanalysis of ocean climate using Simple Ocean Data Assimilation (SODA). Mon. Weather Rev., https://doi.org/10.1175/2007MWR1978.1.

Chelton, D. B., M. G. Schlax, and R. M. Samelson, 2011: Global observations of nonlinear mesoscale eddies. Prog. Oceanogr., https://doi.org/10.1016/j.pocean.2011.01.002.

Conkright, M. E., R. a Locarnini, H. E. Garcia, T. D. O'Brien, T. P. Boyer, C. Stepens, and J. I. Antonov, 2002: World Ocean Atlas 2001: Objective analyses, data statistics, and figures CD-ROM documentation. Natl. Oceanogr. Data Cent. Intern. Rep. (NOAA Atlas NESDIS),.

Dee, D. P., and Coauthors, 2011: The ERA-Interim reanalysis: Configuration and performance of the data assimilation system. Q. J. R. Meteorol. Soc., https://doi.org/10.1002/qj.828.

Duhaut, T. H., and D. N. Straub, 2006: Wind stress dependence on ocean surface velocity: Implications for mechanical energy input to ocean circulation. J. Phys. Oceanogr., 36, 202–211, https://doi.org/10.1175/JPO2842.1.

Egbert, G. D., and S. Y. Erofeeva, 2002: Efficient inverse modeling of barotropic ocean tides. J. Atmos. Oceanic Technol., 19, 183–204, https://doi.org/10.1175/1520-0426(2002)019,0183:EIMOBO.2.0.CO;2.

Eliassen, A., and E. Palm, 1960: On the Transfer of Energy in Stationary Mountain Waves. Geofys. Publ.,.

Eyink, G. L., and H. Aluie, 2009: Localness of energy cascade in hydrodynamic turbulence. I. smooth coarse graining. Phys. Fluids, https://doi.org/10.1063/1.3266883.

Ferrari, R., and C. Wunsch, 2009: Ocean circulation kinetic energy: Reservoirs, sources, and sinks. Annu. Rev. Fluid Mech., https://doi.org/10.1146/annurev.fluid.40.111406.102139.

Gill, A. E., J. Green, and A. J. Simmons, 1974: Energy partition in large-scale ocean circulation and production of mid-ocean eddies. Deep-Sea Res. Oceanogr. Abstr., 21, 499–528, https:// doi.org/10.1016/0011-7471(74)90010-2.

Goff, J. A., and T. H. Jordan, 1988: Stochastic modeling of seafloor morphology: Inversion of sea beam data for second-order statistics. J. Geophys. Res., 93, 13 589–13 608, https://doi.org/10.1029/JB093iB11p13589.

Hoskins, B. J., 1974: The role of potential vorticity in symmetric stability and instability. Q. J. R. Meteorol. Soc., https://doi.org/10.1002/qj.49710042520.

Hughes, C. W., and C. Wilson, 2008: Wind work on the geostrophic ocean circulation: An observational study of the effect of small scales in the wind stress. J. Geophys. Res., 113, C02016, https://doi.org/10.1029/2007JC004371.

Ilıcak, M., 2016: Quantifying spatial distribution of spurious mixing in ocean models. Ocean Model., https://doi.org/10.1016/j.ocemod.2016.11.002.

Klymak, J. M., 2018: Nonpropagating form drag and turbulence due to stratified flow over large-scale abyssal hill topography. J. Phys. Oceanogr., 48, 2383–2395, https://doi.org/10.1175/JPO-D-17-0225.1.

——, D. Balwada, A. N. Garabato, and R. Abernathey, 2021: Parameterizing Nonpropagating Form Drag over Rough Bathymetry. J. Phys. Oceanogr., https://doi.org/10.1175/jpo-d-20-0112.1.

——, S. Legg, and R. Pinkel, 2010: High-mode stationary waves in stratified flow over large obstacles. J. Fluid Mech., 644, 321–336, https://doi.org/10.1017/S0022112009992503.

Kunze, E., and R. C. Lien, 2019: Energy sinks for lee waves in shear flow. J. Phys. Oceanogr., https://doi.org/10.1175/JPO-D-19-0052.1.

Large, W. G., J. C. McWilliams, and S. C. Doney, 1994: Oceanic vertical mixing: A review and a model with a nonlocal boundary layer parameterization. Rev. Geophys., 32, 363–403, https://doi.org/10.1029/94RG01872.

Ma, X., and Coauthors, 2016: Western boundary currents regulated by interaction between ocean eddies and the atmosphere. Nature, https://doi.org/10.1038/nature18640.

Marshall, J., A. Adcroft, C. Hill, L. Perelman, and C. Heisey, 1997: A finite-volume, incompressible Navier-Stokes model for studies of the ocean on parallel computers. J. Geophys. Res., 102, 5753–5766, https://doi.org/10.1029/96JC02775.

McWilliams, J. C., M. J. Molemaker, and I. Yavneh, 2004: Ageostrophic, anticyclonic instability of a geostrophic, barotropic boundary current. Phys. Fluids, 16, 3720–3725, https://doi.org/10.1063/1.1785132.

Molemaker, M. J., J. C. McWilliams, and I. Yavneh, 2005: Baroclinic instability and loss of balance. J. Phys. Oceanogr., 35, 1505–1517, https://doi.org/10.1175/JPO2770.1.

Nagai, T., A. Tandon, E. Kunze, and A. Mahadevan, 2015: Spontaneous generation of near-inertial waves by the Kuroshio Front. J. Phys. Oceanogr., 45, 2381–2406, https://doi.org/10.1175/JPO-D-14-0086.1.

Naveira Garabato, A. C., and Coauthors, 2019: Rapid mixing and exchange of deep-ocean waters in an abyssal boundary current. Proc. Natl. Acad. Sci. USA, 116, 13 233–13 238, https://doi.org/10.1073/pnas.1904087116.

Nikurashin, M., and R. Ferrari, 2010a: Radiation and dissipation of internal waves generated by geostrophic flows impinging on small-scale topography: Theory. J. Phys. Oceanogr., 40, 1055–1074, https://doi.org/10.1175/2009JPO4199.1.

——, and ——, 2010b: Radiation and dissipation of internal waves generated by geostrophic flows impinging on smallscale topography: Application to the Southern Ocean. J. Phys. Oceanogr., 40, 2025–2042, https://doi.org/10.1175/2010JPO4315.1.

——, G. K. Vallis, and A. Adcroft, 2013: Routes to energy dissipation for geostrophic flows in the Southern Ocean. Nat. Geosci., 6, 48–51, https://doi.org/10.1038/ngeo1657.

——, and R. Ferrari, 2011: Global energy conversion rate from geostrophic flows into internal lee waves in the deep ocean. Geophys. Res. Lett., https://doi.org/10.1029/2011GL046576.

Saenko, O., X. Zhai, W. Merryfield, and W. Lee, 2012: The combined effect of tidally and eddy-driven diapycnal mixing on the large-scale ocean circulation. J. Phys. Oceanogr., 42, 526–538, https://doi.org/10.1175/JPO-D-11-0122.1.

Salmon, R., 1998: Lectures on Geophysical Fluid Dynamics.

Sen, A., R. B. Scott, and B. K. Arbic, 2008: Global energy dissipation rate of deep-ocean low-frequency flows by quadratic bottom boundary layer drag: Computations from current meter data. Geophys. Res. Lett., 35, L09606, https://doi.org/10.1029/2008GL033407.

Shakespeare, C. J., 2020: Interdependence of internal tide and lee wave generation at abyssal hills: Global calculations. J. Phys. Oceanogr., https://doi.org/10.1175/JPO-D-19-0179.1.

——, and A. M. Hogg, 2017: Spontaneous surface generation and interior amplification of internal waves in a regional-scale ocean model. J. Phys. Oceanogr., 47, 811–826, https://doi.org/10.1175/JPO-D-16-0188.1.

Sheen, K. L., and Coauthors, 2013: Rates and mechanisms of turbulent dissipation and mixing in the Southern Ocean: Results from the Diapycnal and Isopycnal Mixing Experiment in the Southern Ocean (DIMES). J. Geophys. Res. Ocean., https://doi.org/10.1002/jgrc.20217.

Staquet, C., and J. Sommeria, 2002: Internal gravity waves: From instabilities to turbulence. Annu. Rev. Fluid Mech., 34, 559–593, https://doi.org/10.1146/annurev.fluid.34.090601.130953.

Stöber, U., M. Walter, C. Mertens, and M. Rhein, 2008: Mixing estimates from hydrographic measurements in the deep western boundary current of the North Atlantic. Deep-Sea Res. I, 55, 721–736, https://doi.org/10.1016/j.dsr.2008.03.006.

Walter, M., C. Mertens, and M. Rhein, 2005: Mixing estimates from a large-scale hydro-graphic survey in the North Atlantic. Geophys. Res. Lett., 32, L13605, https://doi.org/10.1029/2005GL022471.

Wang, X., Z. Liu, and S. Peng, 2017: Impact of tidal mixing on water mass transformation and circulation in the south China sea. J. Phys. Oceanogr., 47, 419-432, https://doi.org/10.1175/JPO-D-16-0171.1.

Waterman, S., A. C. Naveira Garabato, and K. L. Polzin, 2013: Internal waves and turbulence in the antarctic circumpolar current. J. Phys. Oceanogr., https://doi.org/10.1175/JPO-D-11-0194.1.

Wenegrat, J. O., J. Callies, and L. N. Thomas, 2018: Submesoscale baroclinic instability in the bottom boundary layer. J. Phys. Oceanogr., 48, 2571–2592, https://doi.org/10.1175/JPO-D-17-0264.1.

Williams, P. D., T. W. Haine, and P. L. Read, 2008: Inertia–gravity waves emitted from balanced flow: Observations, properties, and consequences. J. Atmos. Sci., 65, 3543–3556, https://doi.org/10.1175/2008JAS2480.1.

Wright, C. J., R. B. Scott, B. K. Arbic, and D. F. Furnival, 2012: Bottom dissipation of subinertial currents at the Atlantic zonal boundaries. J. Geophys. Res. Ocean., https://doi.org/10.1029/2011JC007702.

Wunsch, C., 1998: The work done by the wind on the oceanic general circulation. J. Phys. Oceanogr., 28, 2332–2340, https://doi.org/10.1175/1520-0485(1998)028,2332:TWDBTW. 2.0.CO;2.

Xu, C., X. Zhai, and X.-D. Shang, 2016: Work done by atmospheric winds on mesoscale ocean eddies. Geophys. Res. Lett., 43, 12 174–12 180, https://doi.org/10.1002/2016GL071275.

Yang, Z., G. Wang, and C. Chen, 2019: Horizontal velocity structure of mesoscale eddies in the South China Sea. Deep. Res. Part I Oceanogr. Res. Pap., 149, https://doi.org/10.1016/j.dsr.2019.06.001.

——, X. Zhai, D. P. Marshall, and G. Wang, 2021: An Idealized Model Study of Eddy Energetics in the Western Boundary “Graveyard.” J. Phys. Oceanogr., https://doi.org/10.1175/jpo-d-19-0301.1.

Zhai, X., and R. J. Greatbatch, 2007: Wind work in a model of the northwest Atlantic Ocean. Geophys. Res. Lett., 34, L04606, https://doi.org/10.1029/2006GL028907.

——, and D. P. Marshall, 2013: Vertical eddy energy fluxes in the North Atlantic subtropical and subpolar gyres. J. Phys. Oceanogr., 43, 95–103, https://doi.org/10.1175/JPO-D-12-021.1.

——, H. L. Johnson, and D. P. Marshall, 2010: Significant sink of ocean-eddy energy near western boundaries. Nat. Geosci., 3, 608–612, https://doi.org/10.1038/ngeo943.